Spin-orbit grating of light in coherent media

Lu Zhao*
School of Physics, Beihang University, Beijing 100191, China

(Received 17 December 2020; accepted 5 November 2021; published 18 November 2021)

We explore the underlying spin-orbit coupling (SOC) mechanism for the interactions between complex structured light fields in a four-level tripod electromagnetically induced transparency (EIT) system. Because one coupling field in the system is a Bessel beam, the susceptibility of the EIT medium can be modulated quasiperiodically in the radial dimension. The paraxial propagation and evolution of a rotating spinor image as the probe field in the medium can be described by a Pauli-like equation with the SOC term. We calculate the spatial distributions of the diffracted patterns of the image in the near field and clearly show the tunable SOC-induced radial splitting of the oppositely polarized pseudospin states. Our scheme may be useful for all-optical processing of spatial multimode signals in coherent media.

DOI: 10.1103/PhysRevA.104.053713

I. INTRODUCTION

Coherent media based on electromagnetically induced transparency (EIT) have been intensively investigated for several decades [1–3]. The EIT and related effects have led to a variety of successful strategies for all-optical manipulation of photons, having potential applications in classical and quantum information processing. For instance, optical diffraction has been considered for the storage and processing of multimode transverse images based on Fourier optics [4–8]. More interestingly, standing-wave light fields can be introduced into the EIT systems to create transverse periodic structures, termed as electromagnetically induced grating (EIG) [9–16]. Such all-optical grating structures can diffract the weak probe laser into a number of discrete directions with high tunability. To further improve the functionality of EIG, diverse configurations have been proposed. In particular, image-induced blazed grating structures can be produced in the EIT systems to deflect the probe laser with very high efficiency (∼98%) [17–20]. Furthermore, Kerr nonlinearity in the EIT systems is utilized to generate sinusoidal phase gratings [21], volume holographic gratings [22,23], and angular vortex gratings [24], etc. Recently, other types of EIG schemes, such as EIG in Rydberg atoms [25,26], polarization-dependent EIG [27], EIG with parity-time symmetry [28–30], have also been widely studied, which could greatly enrich the diffraction phenomena and applications in coherent media.

In recent years, spin-orbit coupling (SOC) of light has attracted considerable attention, which could find a diverse array of applications for spin-orbit photonics at subwavelength scale [31,32]. Furthermore, the SOC of light in the paraxial regime has also been considered for the spatial propagation of a spinor image in the EIT media [33,34]. The giant group refractive index in the EIT media can greatly enhance the SOC strength, thus giving rise to visible spatial quantization of the oppositely polarized pseudospin states. Such an EIT-based scheme offers flexible opportunities to manipulate the SOC of light in an all-optical manner.

In this article, we explore the radially quasiperiodic structures in EIT media, which could be regarded as the spin-orbit grating for a spinor image under rotation. To generate the grating structures, we employ a four-level tripod EIT system with ultracold atoms and use Bessel beams in one of the coupling fields. We investigate the spatial evolution of the spinor image through the spin-orbit grating using different EIT parameters, where the pseudospin states can undergo SOC-induced radial splitting by diffraction. Our work shows the underlying SOC mechanism for the interactions between complex structured light fields in coherent media, having potentials in multidimensional optical information processing and coding.

II. THEORETICAL MODEL

As shown in Fig. 1, the four-level tripod system contains one weak probe light field and two strong coupling light fields. The probe light field is a spinor image composed of two Laguerre-Gaussian (LG) modes with opposite orbital angular momentum (OAM) indices $\pm\ell$ [35]. One coupling field is a Bessel beam [36,37] and the other is an expanded Gaussian beam. To rotate the spinor image at the frequency of Ω, one can pass the image through a rotating Dove prism with the rotation frequency $\Omega/2$ [38] or introduce the frequency shifts $\pm\ell\Omega$ into the $\pm\ell$ LG modes [39,40], respectively. There are three ground states $|1\rangle$, $|2\rangle$, and $|3\rangle$ and one excited state $|4\rangle$ in the tripod system. Without rotation, the probe image interacts with the atomic transition $|1\rangle \leftrightarrow |4\rangle$ with single-photon detuning $\Delta_p = \omega_p - \omega_{41}$. The coupling C1 (C2) field drives the atomic transition $|2\rangle \leftrightarrow |4\rangle$ ($|3\rangle \leftrightarrow |4\rangle$) with single-photon detuning $\Delta_{c1} = \omega_{c1} - \omega_{42}$ ($\Delta_{c2} = \omega_{c2} - \omega_{43}$). Upon rotation, the two LG modes in the spinor image can achieve opposite rotational Doppler shifts $\pm\ell\Omega$, respectively. Under the rotating-wave and electric-dipole approximations, the in-

*zhaol@buaa.edu.cn

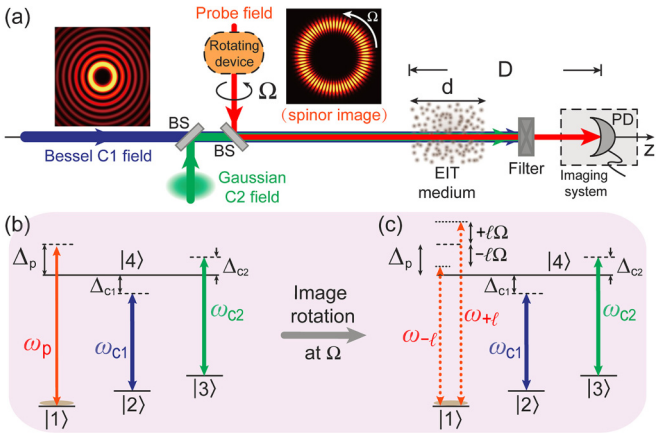

FIG. 1. (a) Schematic setup for the all-optical spin-orbit grating of light in an EIT system, where the spinor image rotates at a frequency of Ω. The image hits the medium at its waist, then propagates a distance of D to the photodetector (PD). The thickness of the medium is d. A Bessel (expanded Gaussian) beam can be applied as the strong coupling C1 (C2) field. The image, C1, and C2 fields are colinear and copropagating. (b) A four-level tripod EIT system without image rotation, where $|1\rangle$, $|2\rangle$, and $|3\rangle$ are the ground states and $|4\rangle$ is the excited state. (c) Upon rotation, the two LG modes undergo opposite rotational Doppler shifts $\pm\ell\Omega$ and interact with the $|1\rangle \leftrightarrow |4\rangle$ transition, where $\omega_{\pm\ell} = \omega_p \pm \ell\Omega$. Note that, in panel (c), we use Δ_p in the nonrotation case in panel (b) as a reference of the frequency detuning and attach $\pm\ell\Omega$ as two additional rotational frequency shifts originating from the image rotation.

teractions between the complex structured light fields and the ultracold atoms in the tripod EIT system can be described by the time-dependent Hamiltonian [41]

$$\begin{aligned}\mathscr{H} = &-\hbar(\Delta_p|4\rangle\langle 4| + \delta'|2\rangle\langle 2| + \delta''|3\rangle\langle 3|) \\ &- \hbar[\Omega_p|4\rangle\langle 1| + \Omega_{c1}|4\rangle\langle 2| + \Omega_{c2}|4\rangle\langle 3| + \text{H.c.}], \end{aligned} \quad (1)$$

where $\delta' = \Delta_p - \Delta_{c1}$ and $\delta'' = \Delta_p - \Delta_{c2}$ are the two-photon detunings in the absence of rotation (i.e., $\Omega = 0$), $\Omega_p = \Omega_{+\ell}e^{-i\ell\Omega t} + \Omega_{-\ell}e^{+i\ell\Omega t}$ is the effective probe Rabi frequency with $\Omega_{\pm\ell}$ the Rabi frequencies of the LG modes in the spinor image, and Ω_{c1} (Ω_{c2}) is the Rabi frequency of the coupling C1 (C2) field. Consequently, the light-atom interactions in the tripod EIT system are governed by the time-dependent density-matrix master equation $\dot{\rho} = -i[\mathscr{H}, \rho]/\hbar + \mathcal{L}\rho$, where $\dot{\rho}$ denotes the derivative of ρ with respect to time and the operator $\mathcal{L}$ phenomenologically describes all the spontaneous decay and decoherence processes.

The response of the atomic system to the three light fields can be derived from the well-known density matrix formalism. Thus, we can obtain the equations of motion for some matrix elements in the atomic density operator as follows:

$$\dot{\rho}_{21} = (-\gamma_{21} + i\delta')\rho_{21} - i\Omega_p\rho_{24} + i\Omega_{c1}^*\rho_{41}, \quad (2a)$$

$$\dot{\rho}_{31} = (-\gamma_{31} + i\delta'')\rho_{31} - i\Omega_p\rho_{34} + i\Omega_{c2}^*\rho_{41}, \quad (2b)$$

$$\begin{aligned}\dot{\rho}_{41} = &(-\gamma_{41} + i\Delta_p)\rho_{41} + i\Omega_{c1}\rho_{21} + i\Omega_{c2}\rho_{31} \\ &- i\Omega_p(\rho_{44} - \rho_{11}). \end{aligned} \quad (2c)$$

The coherence decay rate between levels $|4\rangle$ and $|1\rangle$ can be given by $\gamma_{41} = (\Gamma_{41} + \Gamma_{42} + \Gamma_{43})/2$, where Γ_{4i} denote the radiative decay rates of the populations from level $|4\rangle$ to $|i\rangle$ ($i = 1, 2, 3$) [42]. And, we ignore the coherence decay associated with inhomogeneous broadening (e.g., Doppler broadening) in the cold atomic ensemble as done in Ref. [9].

Note that, when the spinor image rotates at the frequency of Ω, the petal-shaped pattern actually scans azimuthally in the cold atomic cloud. Therefore, the individual off-axis atoms in the cloud experience an amplitude-modulated field (*pulse train*) generated by the rotating (bichromatic) probe light field with the carrier (central) frequency $(\omega_{+\ell} + \omega_{-\ell})/2 = \omega_p$ and the modulation frequency $\Delta\omega = (\omega_{+\ell} - \omega_{-\ell})/2 = \ell\Omega$ where $\omega_{\pm\ell} = \omega_p \pm \ell\Omega$ with $\ell\Omega \ll \omega_p$ are the angular frequencies of the $\pm\ell$ modes under rotation, i.e., two Fourier frequencies in the pulse train (see Figs. 1(b) and 1(c), and some related work, e.g., in Refs. [39,43,44]). (The on-axis intensity of the probe image is always zero due to the phase singularity of the LG modes.) Consequently, based on Ref. [43], for the light-atom interactions, our scheme can also be viewed as a slow-light model for the pulsed probe field in the EIT systems. (For example, see Appendices A and B for some formal derivations based on the slow-light model.) In what follows, we thus adopt some approximations widely used in the EIT systems for slow-light studies.

We first assume that the atoms are initially prepared in level $|1\rangle$ and other levels are empty. Also, the probe field is so weak that its intensity is much lower than the saturation intensity of the $|1\rangle \leftrightarrow |4\rangle$ transition. Therefore, we can assume that the populations of the atomic levels are $\rho_{11} \approx 1$ and $\rho_{22} \approx \rho_{33} \approx \rho_{44} \approx 0$ and ignore the second-order small quantities $\Omega_p\rho_{24}$ and $\Omega_p\rho_{34}$ in Eqs. (2) (e.g., see Ref. [42] and Appendix C for details).

Moreover, because the effective probe Rabi frequency Ω_p is time-dependent, we resort to the Floquet method for polychromatic fields to analytically solve Eqs. (2) [45]. To this end, the matrix elements should be decomposed into Fourier harmonics as

$$\rho_{j1}(t) = \sum_{m=-\infty}^{+\infty} \rho_{j1}^{(m)}(t)e^{im\ell\Omega t} \quad (j = 2, 3, 4), \quad (3)$$

where $\ell\Omega$ is the magnitude of the rotational Doppler frequency shift.

Consequently, by substituting Eqs. (3) into Eqs. (2) and equating the coefficients of the harmonics of $\ell\Omega$, one can achieve a closed set of the equations for the $\pm$1st order components of the elements ρ_{21}, ρ_{31}, and ρ_{41}, which are associated with the $\pm\ell$ LG modes. The equations take the form of

$$\dot{\rho}_{21}^{(\mp1)} = (-\gamma_{21} + i\delta'_{\pm\ell})\rho_{21}^{(\mp1)} + i\Omega_{c1}^*\rho_{41}^{(\mp1)}, \quad (4a)$$

$$\dot{\rho}_{31}^{(\mp1)} = (-\gamma_{31} + i\delta''_{\pm\ell})\rho_{31}^{(\mp1)} + i\Omega_{c2}^*\rho_{41}^{(\mp1)}, \quad (4b)$$

$$\begin{aligned}\dot{\rho}_{41}^{(\mp1)} = &(-\gamma_{41} + i\Delta_{\pm\ell})\rho_{41}^{(\mp1)} + i\Omega_{c1}\rho_{21}^{(\mp1)} \\ &+ i\Omega_{c2}\rho_{31}^{(\mp)} + i\Omega_{\pm\ell}, \end{aligned} \quad (4c)$$

where $\delta'_{\pm\ell} = \delta' \pm \ell\Omega$, $\delta''_{\pm\ell} = \delta'' \pm \ell\Omega$, and $\Delta_{\pm\ell} = \Delta_p \pm \ell\Omega$. By setting the terms $\dot{\rho}_{21}^{(\mp1)}$, $\dot{\rho}_{31}^{(\mp1)}$, and $\dot{\rho}_{41}^{(\mp1)}$ on the left side to

be zero, one can achieve the steady-state solutions of Eqs. (4) with respect to $\rho_{21}^{(\mp1)}$, $\rho_{31}^{(\mp1)}$, and $\rho_{41}^{(\mp1)}$ (see Appendix D for other-order terms with $\mathfrak{m} \neq \pm1$). Thus, the linear susceptibilities of the $\pm\ell$ modes in the probe field can be expressed as

$$\chi(\omega_{\pm\ell}) = \frac{\mathcal{N}\mu_{14}^2}{\hbar\epsilon_0}\frac{\rho_{41}^{(\mp1)}}{\Omega_{\pm\ell}} = \frac{i\mathcal{N}\mu_{14}^2}{\hbar\epsilon_0}\Bigg[(\gamma_{41} - i\Delta_{\pm\ell}) + \frac{|\Omega_{c1}|^2}{(\gamma_{21} - i\delta'_{\pm\ell})} + \frac{|\Omega_{c2}|^2}{(\gamma_{31} - i\delta''_{\pm\ell})}\Bigg]^{-1}, \tag{5}$$

where $\mathcal{N}$ is the atomic number density, μ_{14} is the electric dipole moment of the $|1\rangle \leftrightarrow |4\rangle$ transition, $\hbar$ is the reduced Planck's constant, and ϵ_0 is the vacuum permittivity.

Consider the ideal EIT system with $\gamma_{21(31)} \approx 0$, we also assume that, in the absence of the image rotation (i.e., $\Omega = 0$), all the light fields are resonant with the corresponding atomic transitions. Upon the image rotation (i.e., $\Omega \neq 0$), the coupling fields satisfy the near-resonance EIT conditions $|\Omega_{c1}|^2 + |\Omega_{c2}|^2 \gg \{\ell\Omega\gamma_{41}, \ell^2\Omega^2\}$. Thus, to first order of Ω/ω_p, the susceptibilities can be simplified as

$$\chi(\omega_{\pm\ell}) \approx \frac{\mathcal{N}\mu_{14}^2}{\hbar\epsilon_0}\frac{\pm\ell\Omega}{|\Omega_{c1}|^2 + |\Omega_{c2}|^2} + O(\Omega^3) = 2(n_g - 1)\frac{\pm\ell\Omega}{\omega_p} + O(\Omega^3), \tag{6}$$

where $n_g = 1 + \frac{\mathcal{N}\mu_{14}^2\omega_p}{2\hbar\epsilon_0(|\Omega_{c1}|^2+|\Omega_{c2}|^2)}$ is the group refractive index for an ideal on-resonance EIT scheme. Note that, in the near-resonant EIT systems, the phase refractive index n is near-unity. Thus, we usually have $n_g \gg n \approx 1$. Also, it is clearly seen that the group refractive index n_g can be modulated by two coupling fields while the absorption can be suppressed, offering high flexibility to realize all-optical manipulation of light.

In the EIT system, the paraxial propagation of the two LG modes are governed by two Schrödinger-type equations $2ik_{\pm\ell}\partial\mathcal{E}_{\pm\ell}/\partial z = -\nabla_{r,\phi}^2\mathcal{E}_{\pm\ell} - k_{\pm\ell}^2\chi(\omega_{\pm\ell})\mathcal{E}_{\pm\ell}$, where the operator $\nabla_{r,\phi}^2$ is the sum of the radial and azimuthal Laplacians and $\mathcal{E}_{\pm\ell}$ are the slow-varying amplitudes of the two modes. The two equations can be combined as $2ik_{\pm\ell}\partial\Psi/\partial z = -\nabla_{r,\phi}^2\Psi - k_{\pm\ell}^2\chi(\omega_{\pm\ell})\Psi$, where the spinor wave function $\Psi = (\mathcal{E}_{+\ell}, \mathcal{E}_{-\ell})^T = (\mathcal{A}_+e^{+i\ell\phi}, \mathcal{A}_-e^{-i\ell\phi})^T$ under rotational invariance, $\mathcal{A}_\pm$ stand for the radial wave functions, and $e^{\pm i\ell\phi}$ are the helical phase profiles. Using the unitary transformation $\Phi = \hat{U}\Psi$ with $\hat{U} = \begin{pmatrix}1 & 0\\ 0 & e^{2i\ell\phi}\end{pmatrix}$, we have $\Phi = e^{i\ell\phi}(\mathcal{A}_+, \mathcal{A}_-)^T = e^{i\ell\phi}(\mathcal{A}_+|+_z\rangle + \mathcal{A}_-|-_z\rangle)$ as the spin-orbit spinor, where $e^{i\ell\phi}$ is the orbital wave function and $|\pm_z\rangle$ represent the pseudo-spin-up and -down states.

Accordingly, the two combined Schrödinger-type equations can then be mapped into a Pauli-like equation with the SOC term under rotational invariance, which can be expressed as

$$i\frac{\partial}{\partial z}\Phi = \left(-\frac{1}{2}k^{-1}\nabla_{r,\phi}^2 - \zeta\hat{\ell}\hat{\sigma}_z - \zeta\ell - \zeta\ell^2\frac{\Omega}{\omega_p}\right)\Phi. \tag{7}$$

In Eq. (7), we have $k^{-1} = \begin{pmatrix}1/k_{+\ell} & 0\\ 0 & 1/k_{-\ell}\end{pmatrix}$ is similar to a mass operator, $k_{\pm\ell} = \omega_{\pm\ell}/c = (\omega_p \pm \ell\Omega)/c$ are the wave vectors of the rotating LG modes. The operator $\hat{\ell} = -i\partial_\phi$ is the OAM z-component operator, $\hat{\sigma}_z$ is the third Pauli matrix, $\hat{\ell}\hat{\sigma}_z$ thus denotes the Russell-Saunders-type SOC. As a result, the coefficient $\zeta \approx (n_g - 1)\Omega/c$ can be defined as the SOC strength for $\ell\Omega \ll \omega_p$ and is consistent with the "specific rotary power" for a slow-light medium with $n_g \gg n \approx 1$ [44,46]. The last two terms stand for the "energy shifts" associated with the OAM index ℓ and have nothing to do with spin states. Note that, under the condition of $\ell\Omega \ll \omega_p$, the last term $\zeta\ell^2\Omega/\omega_p$ could be ignored. Consequently, Eq. (7) is isomorphic to the two combined Schrödinger-type equations mentioned before, where the radial evolution of the two LG modes can represent that of the pseudo-spin-up and -down states $|\pm_z\rangle$ affected by the SOC effect.

Taking advantage of such excellent and peculiar properties of EIT media, we can introduce a Bessel beam in the coupling C1 field and an expanded Gaussian beam in the coupling C2 field to keep the rotational invariance of the system (see Fig. 1), and further investigate the interactions between complex structured light fields via atomic ensembles for visualizing and analyzing the underlying SOC mechanism for all-optical diffraction.

III. NUMERICAL RESULTS AND ANALYSIS

Note that, in atomic physics, the studies on the SOC effect focus mainly on the energy splitting for the electronic levels in an atom because it can be experimentally characterized by atomic spectrum. Moreover, the SOC could also lift the spatial degeneracy of the wave functions of different spin states, which can hardly be observed in an atom. In the following, we will demonstrate the SOC-related effect by numerically calculating the lifting of spatial degeneracy of the pseudospin wave functions $|\pm_z\rangle$ in the spinor image.

Moreover, Bessel beams have attracted much attention for decades due to their unique nondiffractive nature [36,37]. In practice, it is possible to approximately generate Bessel beams in experiments, which can sustain the diffraction-free properties over a long distance. Therefore, for cold atomic clouds with finite size, we assume the Rabi frequency of the Bessel C1 field as $\Omega_{c1} = \mathring{\Omega}_{c1}J_b(k_r r)\exp(ib\phi)$, where $\mathring{\Omega}_{c1}$ is a real scale value, J_b denotes the bth-order Bessel function with b an integer, k_r is the radial component of the wave vector. For high-order Bessel beams ($b > 1$), the central intensity at $r = 0$ vanishes due to the phase singularity associated with the azimuthal phase term $\exp(ib\phi)$.

In addition, for the coupling C2 field, we employ an expanded Gaussian beam. Its Rabi frequency is given by $\Omega_{c2} = \mathring{\Omega}_{c2}\exp(-r^2/w_{c2}^2)$, where $\mathring{\Omega}_{c2}$ is the peak value and w_{c2} is the waist width. In this way, the total coupling intensity ($\propto |\Omega_{c1}|^2 + |\Omega_{c2}|^2$) does not vanish in the interaction region to ensure the validity of the near-resonance EIT conditions in Eq. (6). As a result, the Bessel C1 field with $|\Omega_{c1}|^2 = \mathring{\Omega}_{c1}^2J_n^2(k_r r)$ can lead to a quasiperiodic SOC strength ζ in the radial dimension. Such an EIT system can also be regarded as a spin-orbit grating to diffract the spinor image in free space.

To visualize the spatial results of the SOC-based diffraction induced by the EIT system with a set of concentric ring structures in Fig. 1(a), we can utilize the split-step method to

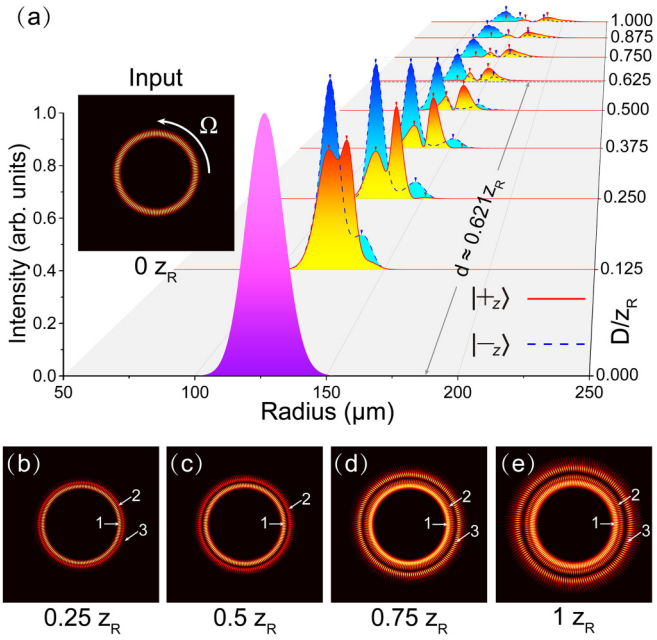

FIG. 2. (a) Intensity evolution (in arbitrary units) of the pseudospin $|\pm_z\rangle$ states (i.e., the two LG modes) propagating in space. The arrows mark the peak positions. Inset: A snapshot of the input image with $\pm\ell = \pm 80$ at the waist ($D = 0$), which rotates at $\Omega = 60$ Hz. Bottom: snapshots of the intensity patterns of the rotating image at different propagation distances for (b) $D = 0.25z_R$, (c) $0.5z_R$, (d) $0.75z_R$, and (e) $1z_R$, where the size of the pictures is $500 \times 500\ \mu\text{m}^2$. The peak values of the patterns are normalized and all the ring structures are labeled. Optical parameters: $w_0 = 20\ \mu$m for the LG modes and $z_R = \pi w_0^2/\lambda_p \approx 1.611$ mm is the Rayleigh range acting as a scaling parameter for the propagation distance D; $\mathring{\Omega}_{c1} = \gamma_{41}$, $k_r = 0.15\ \mu\text{m}^{-1}$, and $b = 15$ for the Bessel C1 field; $\mathring{\Omega}_{c2} = 0.12\gamma_{41}$ and $w_{c2} = 1$ mm for the Gaussian C2 field. The longitudinal range of the EIT medium is also labeled by the gray dashed line, where the thickness $d = 1$ mm $\approx 0.621z_R$.

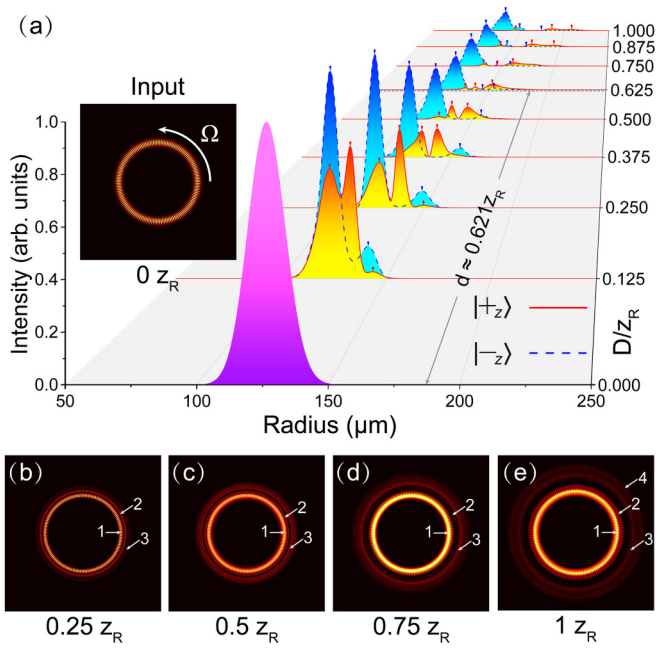

FIG. 3. (a) Intensity evolution of the pseudospin $|\pm_z\rangle$ states in space. Inset: a snapshot of the input image at the waist, which rotates at $\Omega = 100$ Hz. Bottom: Snapshots of the rotating image at different propagation distances for (b) $D = 0.25z_R$, (c) $0.5z_R$, (d) $0.75z_R$, and (e) $1z_R$. Except the rotation frequency, all other parameters are the same as those in Fig. 2.

solve Eq. (7). The incident spinor image at $D = 0$ is given by

$$\Phi = C_0 \sqrt{\frac{2}{\pi w_0^2 \ell!}} \left(\frac{\sqrt{2}r}{w_0}\right)^{\ell} e^{-\frac{r^2}{w_0^2}} e^{i\ell\phi} \begin{pmatrix} 1 \\ 1 \end{pmatrix}, \tag{8}$$

where C_0 is the normalization constant and w_0 is the waist width of the LG modes [35].

For the EIT system, we adopt ultracold ^{87}Rb atomic ensemble and the D2 line to construct the tripod configuration. We assume the atomic number density $\mathcal{N} \approx 10^{12}$ cm^{-3}, the decay and decoherence rates $\gamma_{41} = 2\pi \times 6$ MHz and $\gamma_{31} = \gamma_{21} = 2\pi \times 1$ kHz, and the dipole moment $\mu_{14} = 3.58 \times 10^{-29}$ Cm [47]. The thickness of the EIT medium is $d = 1$ mm. For the light fields, the wavelengths of the probe, Bessel C1, and Gaussian C2 fields are $\lambda_p \approx \lambda_{c1} \approx \lambda_{c2} \approx 780$ nm.

In Fig. 2, the coupling C1 field is a high-order Bessel beam with $\mathring{\Omega}_{c1} = \gamma_{41}$, $k_r = 0.15\ \mu\text{m}^{-1}$, and $b = 15$. The coupling C2 field is an expanded Gaussian beam with $\mathring{\Omega}_{c2} = 0.12\gamma_{41}$ and $w_{c2} = 1$ mm. For low rotation frequency, we may use a rotating Dove prism with a rotation frequency of 30 Hz. Thus, the rotation frequency of the image is $\Omega = 60$ Hz. To increase the rotational Doppler effect, the LG modes with high OAM indices $\pm\ell = \pm 80$ are adopted to generate the spinor image, where the waists of both LG modes are equal (e.g., $w_0 = 20\ \mu$m). It is seen that different spatial evolution can occur for the two pseudospin states (i.e., the two LG modes) in Fig. 2(a), where the SOC causes spatial separation of the two pseudospin states in the radial direction. For the $|+_z\rangle$ state, double-peak structures can be produced in the radial direction at the propagation distances $D = 0.125z_R$ and $0.5z_R$ and weak triple-peak structures appear at $D = 0.25z_R$, $0.375z_R$, and $D \geqslant 0.625z_R$. For the $|-_z\rangle$ state, double-peak structures are maintained for $D \leqslant 0.5z_R$, while weak triple-peak structures appear from $D = 0.625z_R$ to z_R. Relatively, the intensity of the pseudospin $|+_z\rangle$ state expands outwards, while that of the pseudospin $|-_z\rangle$ state shrinks inwards. We also can see the corresponding 2D images in Fig. 2. As shown in the inset of Fig. 2(a), the input intensity distribution has a petal-wheel-like pattern of 160 maxima in a single ring. The SOC-induced splitting of the $|\pm_z\rangle$ states leads to double-ring [i.e., rings 1 and 2 in Fig. 2(c)] and weak triple-ring structures [i.e., rings 1, 2, and 3 in Figs. 2(b), 2(d), and 2(e)], still having the petal-wheel-like patterns in the azimuthal direction. (Note that the outermost ring 3 in Fig. 2(b) is very weak.)

To enhance the effect, we increase the rotation frequency of the image to $\Omega = 100$ Hz by raising the rotation frequency of the Dove prism to 50 Hz and keep all the other parameters unchanged in Fig. 3. We can see that, at the same propagation distance, the double-peak or triple-peak structures become more significant in Fig. 3(a). At certain positions (e.g., $D \leqslant 0.5z_R$), compared with those in Fig. 2(a), the dip between the two peaks of $|-_z\rangle$ state becomes deeper and wider and

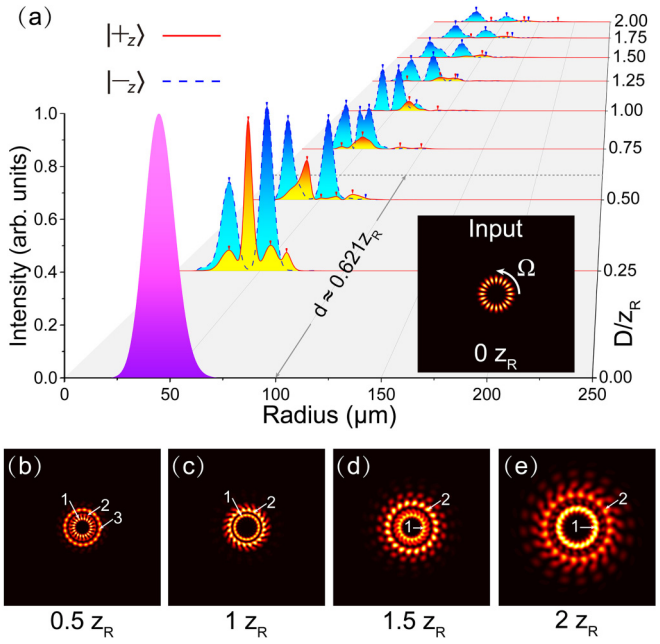

FIG. 4. (a) Intensity evolution of the pseudospin $|\pm_z\rangle$ states in space. Inset: a snapshot of the input image with $\pm\ell = \pm 10$ at the waist, which rotates at $\Omega = 800$ Hz. Bottom: snapshots of the rotating image at different propagation distances for (b) $D = 0.5z_R$, (c) $1z_R$, (d) $1.5z_R$, and (e) $2z_R$. Note that, for simplicity, only the rings with low fringe contrast are labeled. Optical parameters: $w_0 = 20$ μm; $\mathring{\Omega}_{c1} = \gamma_{41}$, $k_r = 0.15$ μm^{-1}, and $b = 3$ for the Bessel C1 field; $\mathring{\Omega}_{c2} = 0.12\gamma_{41}$ and $w_{c2} = 1$ mm for the Gaussian C2 field.

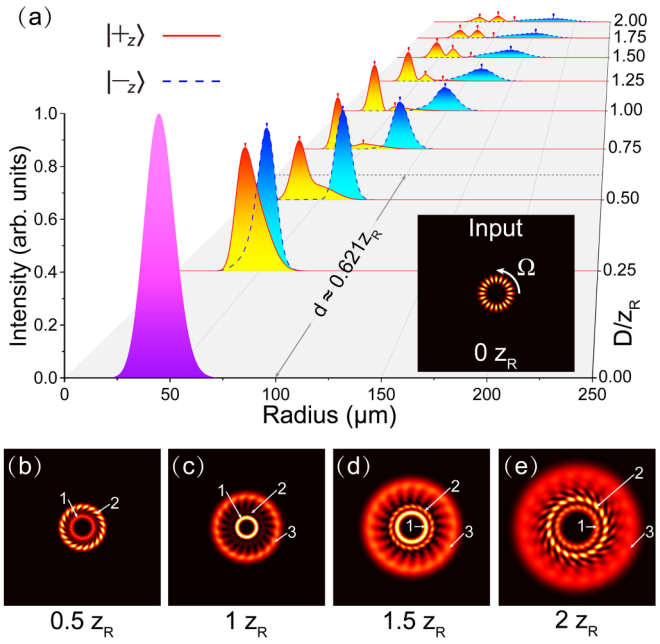

FIG. 5. (a) Intensity evolution of the pseudospin $|\pm_z\rangle$ states in space. Inset: A snapshot of the input image with $\pm\ell = \pm 10$ at the waist, which rotates at $\Omega = 2000$ Hz. Bottom: snapshots of the rotating image at different propagation distances for (b) $D = 0.5z_R$, (c) $1z_R$, (d) $1.5z_R$, and (e) $2z_R$. Optical parameters: $w_0 = 20$ μm; $\mathring{\Omega}_{c1} = 2\gamma_{41}$, $k_r = 0.1$ μm^{-1}, and $b = 6$ for the Bessel C1 field; $\mathring{\Omega}_{c2} = 0.2\gamma_{41}$ and $w_{c2} = 1$ mm for the Gaussian C2 field.

thus one peak of the $|+_z\rangle$ state can well stay in the dip. Also, for $D \geqslant 0.625z_R$, the innermost peak of the $|-_z\rangle$ state becomes strongly predominant. These distinctions can also be shown in the 2D intensity patterns. In Fig. 3(b), the outermost ring 3 of the triple-ring structure is slightly augmented. The contrast of the petal-wheel-like fringes in the middle ring 2 is weakened because, at this ring position, the $|+_z\rangle$ state with a peak dominates over the $|-_z\rangle$ state with a wide dip. Similar situations occur for Figs. 3(c)–3(e), where the fringe contrast of the inner rings 1 becomes low, particularly for ring 1 in Fig. 3(d), because the inner peaks of the $|-_z\rangle$ state are predominant as aforementioned. Consequently, by spatial filtering, one may select the desired pseudospin state from the diffraction pattern.

By introducing the frequency shifts $\pm\ell\Omega$ into the $\pm\ell$ LG modes, respectively, one can rotate the image with higher speed. In Fig. 4, the image rotation frequency is $\Omega = 800$ Hz. Accordingly, we lower the OAM indices of the LG modes to $\pm\ell = \pm 10$ and also lower the order of the Bessel beam in the C1 field to $b = 3$. Quadruple-peak structures appear in the $|+_z\rangle$ state at some short propagation distances (e.g., $D = 0.25z_R$, $0.5z_R$, and $0.75z_R$). At farther distances, some minor peaks gradually weaken due to absorption and diffraction-induced energy spread in space. For the $|-_z\rangle$ state, the intensity profile has double-peak structures at short propagation distances ($D = 0.25z_R$ and $0.5z_R$) and triple-peak structures for longer distances (from $D = 0.75z_R$ to $2z_R$), where the outermost peak fades out during propagation. For the 2D intensity patterns, we have the petal-wheel-like pattern of 20 maxima in a single ring for the input image in the inset of Fig. 4(a). In Fig. 4(b), there are three rings with low fringe contrast, where the inner and outer rings (1 and 3) predominantly originate from the $|-_z\rangle$ state and the middle ring 2, though very thin, comes from the $|+_z\rangle$ state. In Figs. 4(c)–4(e), we can clearly see two rings 1 and 2 with low fringe contrast, to which the two inner peaks of the $|-_z\rangle$ state contribute mostly. (Note that, for simplicity, the rings with high fringe contrast are not labeled.)

In Fig. 5, we increase the image rotation frequency to $\Omega = 2000$ Hz. We also change the parameters of the Bessel C1 field to $k_r = 0.1$ μm^{-1} and $b = 6$. To suppress the absorption, we increase the intensity parameters of the two coupling fields to $\mathring{\Omega}_{c1} = 2\gamma_{41}$ and $\mathring{\Omega}_{c2} = 0.2\gamma_{41}$. As seen, large spatial separation can be achieved. Contrary to the trend in Figs. 2–4, the $|+_z\rangle$ state in Fig. 5(a) shrinks inwards but the $|-_z\rangle$ state expands outwards. In details, the $|+_z\rangle$ state has single-peak structures at $D = 0.25z_R$, double-peak structures at $D = 0.5z_R$, $0.75z_R$ and $1z_R$, and weak triple-peak structures in the range from $D = 1.25z_R$ to $2z_R$, while the $|-_z\rangle$ state keeps a single peak during propagation. Accordingly, turbine-wheel-like patterns with well-separated rings appear in Figs. 5(b)–5(e). Due to the large spatial separation, the fringe contrast in the ring structures becomes very low. In Figs. 5(b), the $|+_z\rangle$ ($|-_z\rangle$) state dominates the inner ring 1 (outer ring 2). In Figs. 5(c)–5(e), the $|+_z\rangle$ state dominates the two inner rings 1 and 2, corresponding to the two innermost strong peaks in Fig. 5(a) at $D = 1z_R$, $1.5z_R$ and $2z_R$. The $|-_z\rangle$ state always dominates the outer ring 3, though, radially broadened by diffraction.

Note that, Figs. 2–5 actually show the spatial consequence of the SOC effect, i.e., the radial splitting of the wave functions of the pseudospin states (i.e., the two LG modes) in the radial dimension. Strictly speaking, the SOC of the spinor image only occurs *inside the EIT medium* because, in the medium, we can achieve the group refractive index $n_g \gg 1$ and thus the SOC strength ζ can be greatly enhanced [see Eq. (7)]. To clarify this point, in Figs. 2–5, we label the longitudinal regions to explicitly show the range of the EIT medium.

However, the SOC of the spinor image in the medium will definitely influence the free-space evolution of the image behind the medium. We thus show the evolution of the image in the ranges for $d < D \leqslant 1z_R$ in Figs. 2 and 3 and for $d < D \leqslant 2z_R$ in Figs. 4 and 5, where d is the thickness of the medium. In optics, the free-space evolution of the image closely behind the medium can also be considered as the near-field diffraction of the spinor image. This is the reason why we call the radially quasiperiodic structure as "spin-orbit grating" in our scheme. In practice, it is difficult to directly observe the spatial evolution of the spinor image inside the EIT medium. But, the near-field diffraction pattern behind the medium can serve as a practical means to characterize the SOC-induced splitting of the pseudospin states inside the EIT medium.

IV. DISCUSSION

A. The presence of single-photon detuning Δ_p for nonrotating spinor image

In Eqs. (1)–(5), we first achieve the general expressions to describe the light-atom interactions in the EIT system. To obtain Eq. (6), we consider a typical EIT scheme. In this scheme, when the spinor image in the probe field does not rotate (i.e., $\Omega = 0$), all the light fields are resonant with the corresponding atomic transitions (i.e., $\Delta_p = \Delta_{c1} = \Delta_{c2} = 0$ for a resonant EIT system), leading to a symmetric EIT transmission window. When the spinor image is rotating at the frequency of Ω, the frequencies of the two LG modes symmetrically shift away from the resonance by $\pm\ell\Omega$, respectively. Therefore, Eq. (6) includes the single-photon detunings of the two LG modes in the rotating spinor image as $\Delta_{\pm\ell} = \pm\ell\Omega$.

When $\Delta_p \neq 0$, as long as the near-resonance EIT conditions $|\Omega_{c1}|^2 + |\Omega_{c2}|^2 \gg \{\Delta_{\pm\ell}\gamma_{41},\ \Delta_{\pm\ell}^2\}$ are satisfied, the susceptibilities in Eq. (6) for an ideal EIT system with $\gamma_{21(31)} \approx 0$ and $\Delta_{c1} = \Delta_{c2} = 0$ can be rewritten as

$$\begin{aligned}\chi(\omega_{\pm\ell}) &\approx \frac{\mathcal{N}\mu_{14}^2}{\hbar\epsilon_0}\frac{\Delta_{\pm\ell}}{|\Omega_{c1}|^2 + |\Omega_{c2}|^2} + O\big(\Delta_{\pm\ell}^2\big) \\ &= 2(n_g - 1)\frac{\Delta_{\pm\ell}}{\omega_p} + O\big(\Delta_{\pm\ell}^2\big) \\ &= 2(n_g - 1)\frac{\Delta_p \pm \ell\Omega}{\omega_p} + O\big(\Delta_{\pm\ell}^2\big), \end{aligned} \tag{9}$$

where $n_g = 1 + \frac{\mathcal{N}\mu_{14}^2\omega_p}{2\hbar\epsilon_0(|\Omega_{c1}|^2+|\Omega_{c2}|^2)}$ is the group refractive index same as that in Eq. (6). Compared with Eq. (6), Eq. (9) only has one more term associated with Δ_p ($\neq 0$). For Eq. (7), this new term has no influence on the spin-orbit term and only gives rise to a spin-independent term.

Additionally, to achieve Eq. (6), we actually consider a common slow-light model in the EIT medium, i.e., the resonant EIT scheme. In this case, the central frequency ω_p of the rotating spinor image (*pulse train*) is resonant to the $|1\rangle \leftrightarrow |4\rangle$ transition. Thus, we have $\Delta_p = \omega_p - \omega_{41} = 0$. At the same time, we also assume $\Delta_{c1} = \Delta_{c2} = 0$. Therefore, the central frequencies of the rotating spinor image (*pulse train*), the coupling C1, and C2 fields are all resonant to the corresponding atomic transitions, i.e., all the two-photon detunings are zero. This represents a typical slow-light EIT system having a very important property that the second-order term of Ω in Eq. (6) vanishes exactly. Consequently, there is no group velocity dispersion of the rotating spinor image (*pulse train*) through the EIT medium. (Also see Secs. III and IV in the review paper Ref. [3] for the slow-light propagation.)

B. Diffraction capability of the spin-orbit grating

In this work, we term the radially quasiperiodic structure in the EIT medium "spin-orbit grating." Usually for grating structures in optics, the discrete diffraction peaks in one or two dimensions is of great importance to demonstrate the optical properties and assess the diffraction capability of gratings (e.g., see Refs. [9–30]). Because the spin-orbit grating in our scheme keeps the rotational invariance, the diffracted field through the grating will spread out in the radial direction, thus generating multiple ring structures. Therefore, we emphasize the discrete peak structures in the radial dimension to keep consistency with the traditional research on optical grating.

However, the diffraction capability of the spin-orbit grating is different from that of traditional gratings without SOC because the spin-orbit grating can separate the two pseudospin states by diffraction. Moreover, because we actually investigate the near-field diffraction of the probe field (e.g., the propagation distance $D \leqslant z_R$ in Figs. 2 and 3 and $D \leqslant 2z_R$ in Figs. 4 and 5), the evolution of the diffracted fields could be rapid and intense. To characterize the spatial evolution in details, we emphasize the peak structures to show the near-field diffraction features of the two LG modes. Additionally, because there lacks an analytical theory for our proposed structures in the EIT system, one has to assess the diffraction capability of the spin-orbit gratings in Figs. 2–5 by using numerical calculations on a case-by-case basis.

In Fig. 2, by observing the intensity profiles in Fig. 2(a) at different propagation distances, one can see that the wave functions of the pseudospin $|\pm_z\rangle$ states (especially, the innermost peaks of the two pseudospin states) cannot separate completely in space. Accordingly, the images in Figs. 2(b)–2(e) are petal-wheel-like patterns with high fringe contrast. As a comparison, in Fig. 3, the separation of the wave functions of the $|\pm_z\rangle$ states is larger than that in Fig. 2. For example, we can see a bright ring-structure with very low fringe contrast at $D = 0.75z_R$ [i.e., ring 1 in Fig. 3(d)], where the innermost peaks of the $|\pm_z\rangle$ states are largely separated. Therefore, at this position of $D = 0.75z_R$, the $|-_z\rangle$ state can be sampled by using a spatial filter. Moreover, the SOC energy can be associated with the frequency difference ($2\Omega\ell$) between the two pseudospin states (i.e., the two LG modes). Because all the parameters are the same in Figs. 2 and 3 except the frequency difference ($2\Omega\ell = 9600$ Hz with $\Omega = 60$ Hz in Fig. 2

and 16 000 Hz with $\Omega = 100$ Hz in Fig. 3), it is seen that larger frequency difference (SOC energy) can lead to higher diffraction capability for the gratings.

In Fig. 4, we change some optical parameters including the OAM indices of LG modes ($\pm\ell = \pm 10$) and the order of the Bessel beam ($b = 3$) and keep the frequency difference between the two pseudospin states still as 16 000 Hz. The innermost peak of the $|-_z\rangle$ state can be separated further away from the $|+_z\rangle$ state. For example, at the positions of $D = 1z_R,\ 1.5z_R,\ 2z_R$ in Figs. 4(c)–4(e), the innermost rings 1 have very low fringe contrast. [Note that, because the image inside the EIT medium can hardly be used to do the spatial filtering in practice, we ignore Fig. 4(b) at $D = 0.5z_R < d$.] Therefore, even if the frequency difference between the two pseudospin states is the same, by changing the light fields, we can also enhance the radial splitting between the two pseudospin states, thus improving the diffraction capability of the grating.

In Fig. 5, we slightly change some optical parameters of the light fields but greatly increase the frequency difference between the two pseudospin states to $2\Omega\ell = 40\,000$ Hz with $\Omega = 2000$ Hz. Consequently, very large spatial separation can be observed in Fig. 5(a), where even the innermost two peaks of the $|+_z\rangle$ state can be separated far away from the $|-_z\rangle$ state. For example, at the positions of $D = 1z_R,\ 1.5z_R,\ 2z_R$ in Figs. 5(c)–5(e), the inner two rings 1 and 2 with very low fringe contrast are dominated by the $|+_z\rangle$ state, while the outer rings 3 represents the $|-_z\rangle$ state. In this case, the two pseudospin states can be sorted by choosing spatial filters with different apertures, showing high diffraction capability.

On the one hand, when all the other parameters are fixed, larger frequency difference (SOC energy) can lead to larger spatial splitting (e.g., see the innermost peaks of the $|\pm_z\rangle$ states in Figs. 2 and 3 as an indicator). On the other hand, by changing the optical parameters, the spatial splitting (e.g., also see the innermost peaks of the $|\pm_z\rangle$ states in Figs. 3 and 4 as an indicator) can also be enhanced even for the same frequency difference. By further increasing the frequency difference and optimizing other optical parameters, very large spatial splitting (e.g., see the innermost two peaks of the $|+_z\rangle$ state and the single peak of the $|-_z\rangle$ state in Fig. 5) can be achieved for the two pseudospin states. Therefore, the frequency difference $2\Omega\ell$ (associated with the SOC energy) plays an indispensable role in creating the diffraction capability. (In other words, without the frequency difference, there is no SOC-related diffraction to split the two pseudospin states.) Meanwhile, other optical parameters in the EIT medium should also be considered to optimize the grating design, which offers the opportunities to manipulate the spin-orbit gratings in an all-optical manner.

C. Near-resonance EIT conditions in Figs. 2–5

Note that the near-resonance EIT conditions $|\Omega_{c1}|^2 + |\Omega_{c2}|^2 \gg \{\ell\Omega\gamma_{41}, \ell^2\Omega^2\}$ used to achieve the static susceptibilities [i.e., Eq. (6)] are also consistent with those in the slow-light model for pulse propagation in EIT systems. These conditions suggest that the two Fourier frequencies in the probe field well stay in the EIT transmission window generated by the coupling C1 and C2 fields (i.e., the modulation frequency $\Delta\omega$ much smaller than the EIT window width) and the susceptibilities are highly linear at the vicinity of the central frequency ω_p, which are also common conditions for EIT-related effects.

Using the parameters in Figs. 2–5, we numerically verify the near-resonance EIT conditions in our work. Note that, because we also have $\gamma_{41} \gg \ell\Omega$ in Figs. 2–5, the condition $|\Omega_{c1}|^2 + |\Omega_{c2}|^2 \gg \ell^2\Omega^2$ can be satisfied automatically in these figures. Apparently, at the dark rings of the Bessel C1 field ($\Omega_{c1} \approx 0$), the expanded Gaussian C2 field (Ω_{c2}) is critical to realize the conditions, which will be considered in the following.

As shown in Figs. 2 and 3, the two LG modes ($\pm\ell = \pm 80$) in the probe field is roughly located within the radius of 175 μm. The Rabi frequency of the C2 field within this range (i.e., $r \lesssim 175\ \mu$m) is given by $\Omega_{c2} = \mathring{\Omega}_{c2}\exp(-r^2/w_{c2}^2) \gtrsim 0.1164\gamma_{41}$, where $\mathring{\Omega}_{c2} = 0.12\gamma_{41}$ and $w_{c2} = 1$ mm. Therefore, even if the Bessel C1 field vanishes at the dark rings, the minimal coupling Rabi frequency experienced by the probe field is determined by the Gaussian C2 field. The transmission window then reads $|\Omega_{c2}|^2/\gamma_{41} \gtrsim 81294$ Hz, while the modulation frequencies are $\ell\Omega = 4800$ Hz in Fig. 2 and 8000 Hz in Fig. 3, respectively. Therefore, the window width is more than an order of magnitude larger than the modulation frequencies. The near-resonance EIT conditions can be satisfied in Figs. 2 and 3.

In Fig. 4, the size of the two LG modes ($\pm\ell = \pm 10$) in the probe field is shrunk and roughly located within the radius of 75 μm. The Rabi frequency of the C2 field within this range (i.e., $r \lesssim 75\ \mu$m) is given by $\Omega_{c2} = \mathring{\Omega}_{c2}\exp(-r^2/w_{c2}^2) \gtrsim 0.1193\gamma_{41}$, where we still have $\mathring{\Omega}_{c2} = 0.12\gamma_{41}$ and $w_{c2} = 1$ mm in Fig. 4. The window width is $|\Omega_{c2}|^2/\gamma_{41} \gtrsim 85395$ Hz, much larger than the modulation frequency $\ell\Omega = 8000$ Hz in Fig. 4.

In Fig. 5, the rotation frequency of the probe field is increased to $\Omega = 2000$ Hz and the peak Rabi frequency of the Gaussian C2 field is raised to $\mathring{\Omega}_{c2} = 0.2\gamma_{41}$. All other parameters in the probe and Gaussian C2 fields are the same as those in Fig. 4. Thus, we can obtain the Rabi frequency of the C2 field within the range of $r \lesssim 75\ \mu$m as $\Omega_{c2} \gtrsim 0.1989\gamma_{41}$. The window width is $|\Omega_{c2}|^2/\gamma_{41} \gtrsim 237\,367$ Hz, again much larger than the modulation frequency $\ell\Omega = 20\,000$ Hz in Fig. 5.

Therefore, the near-resonance EIT conditions are verified in Figs. 2–5, which are also consistent with those in the slow-light model for pulse propagation in EIT systems. Such a fact also ensures that the numerical results of Eq. (7) are reliable in Figs. 2–5.

D. Experimental possibilities

Note that, in our scheme, the $\pm\ell$ LG modes are used to simulate the *radial* evolution of the pseudospin $|\pm_z\rangle$ states, i.e., SOC-induced splitting in the radial dimension. The azimuthal interference fringes of the $\pm\ell$ LG modes are not directly related to the spin $|\pm_z\rangle$ states because, in spin space, the $|\pm_z\rangle$ states are orthogonal and do not interfere in real space. However, the interference fringes can reflect the extent of spatial overlap between the $\pm\ell$ LG modes. For example, owing to the large radial separation in Fig. 5(c), the

contrast of the azimuthal fringes in the inner and outer rings greatly attenuates, which may facilitate the experimental observations.

To rotate the image at low speed, one may use a rotor to mechanically rotate a Dove prism up to ∼167 Hz [48]. Thus, the image rotation frequencies of $\Omega = 60$ Hz in Fig. 2 and $\Omega = 100$ Hz in Fig. 3 are accessible in experiments. For high speed rotation with $\Omega = 800$ Hz in Fig. 4 and $\Omega = 2000$ Hz in Fig. 5, one may introduce the frequency shifts $\pm\ell\Omega$ into the $\pm\ell$ LG modes, respectively, which can produce the image rotation frequency in the range from mHz to MHz [39]. In addition, all the snapshots of single frames in Figs. 2–5 can be captured by a high-speed charge-coupled-device (CCD) imaging system.

Ultracold atomic ensembles with high density and millimeter (even centimeter) size in magneto-optical trap have been successively implemented, in which the EIT-related effects have been observed (e.g., see Ref. [49]). For the D2 line in ^{87}Rb atoms, we can employ the magnetic sublevels in $|5S_{1/2}, F = 1\rangle$ and $|5P_{3/2}, F = 0\rangle$ to construct a closed tripod configuration in Fig. 1, where $|1\rangle$, $|2\rangle$, $|3\rangle$ represent $|5S_{1/2}, F = 1, m_F = -1\rangle$, $|5S_{1/2}, F = 1, m_F = 0\rangle$, $|5S_{1/2}, F = 1, m_F = +1\rangle$, respectively, and $|4\rangle$ stands for $|5P_{3/2}, F = 0, m_F = 0\rangle$ [47]. Also, a magnetic field with moderate strength can be applied to lift the degeneracy of the $|5S_{1/2}, F = 1\rangle$ state. For example, a magnetic field of 15 G can produce a Zeeman splitting of ∼10.5 MHz between adjacent magnetic sublevels in $|5S_{1/2}, F = 1\rangle$. To make sure that each light field only drives one transition, we consider the selection rules for electric dipole transitions and use three laser beams having different polarizations. For example, the probe, Bessel C1, and Gaussian C2 fields could be σ^+, π, and σ^- polarized, respectively.

The structured light fields in the probe and coupling C1 fields can be created by various methods. For example, high-order LG beams can be flexibly generated by liquid-crystal spatial light modulators [50]. Recently, using spiral phase mirrors, very-high-order LG beams with OAM indices up to 10010 can also be obtained [51]. Moreover, by shining strong high-order LG beam on an axicon lens, one can further efficiently generate high-order Bessel beam for the coupling C1 field [37], where the order b of the Bessel beam is determined by that of the incident LG beam. The radial wave vector k_r can be controlled by the the base angle α of the axicon and the refractive index $n_{\rm ax}$ of the axicon material. For $k_r = 0.15$ μm^{-1} used in Figs. 2–4, the base angle of the axicon is given by $\alpha = k_r/[k_{c1}(n_{\rm ax} - 1)] = 2.37^\circ$, where $k_{c1} = 2\pi/\lambda_{c1}$ ($\lambda_{c1} = 780$ nm) is the total wave vector of the Bessel C1 field and $n_{\rm ax} = 1.45$ is the refractive index of the fused silica axicon. For $k_r = 0.1$ μm^{-1} used in Fig. 5, we have the base angle of the axicon $\alpha = 1.58^\circ$. The axicons with such base angles can be customized within current fabrication capabilities for diffractive optical elements.

E. Some comments

First, from the viewpoint of optics, Eq. (6) tells us that, although the frequency (energy) difference between the two LG modes is small, the strong dispersion in the EIT medium can lead to large group refractive index n_g (i.e., the slow-light effect), thus greatly enhancing the SOC strength ζ in Eq. (7). Moreover, note that the susceptibilities in Eq. (6) actually have opposite signs because the two LG modes shift up or down by $\ell\Omega$, respectively, which can produce strong but nearly opposite phase shifts for the two transmitted modes. Besides, compared with the earlier work in Ref. [33], because a Bessel beam can have strong radial intensity variation in its multiring structure, this makes it possible to generate grating structures with steep radial variation (gradient) for the susceptibilities. Therefore, the two LG modes can experience totally different phase modulations with strong optical diffraction through the EIT medium, suggesting the optical origin of the different spatial trajectories of the two LG modes (see Figs. 2–5).

Second, similar to the optical gratings in one or two dimensions in Refs. [9–30], the large spatial separation and discrete multiring structures (i.e., discrete peak structures in the radial direction) in our scheme may offer more opportunities for the applications of all-optical sorting and spatial multiplexing. For example, by using multiple spatial filtering, it is possible to select desired LG modes (i.e., pseudospin states) at different peak (radial) positions, which may improve the flexibility for optical information processing. Also, the peak structures with significant spatial separation may facilitate experimental observations and verifications.

Third, we explore the four-level tripod EIT system, which also represents a major extension of the theoretical model. The two coupling fields could provide higher flexibility for all-optical control over the spinor image in the probe field. In particular, because the Bessel C1 field has vanishing intensity at the dark rings, the EIT conditions cannot be satisfied at these regions for the traditional three-level Λ-type EIT system used in Ref. [33]. However, in a tripod EIT system, the expanded Gaussian C2 field can be used to "fill" the dark regions in the Bessel C1 field to guarantee the near-resonance EIT conditions in Eq. (6), which is critical to derive the Pauli-like equation [i.e., Eq. (7)] to explicitly show the SOC effect.

V. CONCLUSION

In conclusion, we have demonstrated that EIT-based coherent media could establish a flexible platform to visualize the spinor wave function evolution described by a Pauli-like equation. Also, we have investigated the interactions between complex structured light fields in coherent media. The LG modes with opposite OAM indices (i.e., the pseudospin $|\pm_z\rangle$ states) are spatially separated by diffraction as they pass through a radially quasiperiodic grating structure created by a Bessel beam, which can also be termed "spin-orbit grating." Our scheme may help develop promising strategies for spatial information processing of multimode images and vortices in EIT-based coherent media.

ACKNOWLEDGMENTS

L.Z. gratefully thanks F. Peng for helpful discussions. This work was supported by the National Natural Science Foundation of China (Grants No. 11574016 and No. 11204154).

APPENDIX A: A FORMAL DERIVATION OF $\chi(\omega_{\pm\ell})$ BASED ON THE SLOW-LIGHT MODEL

As mentioned in Sec. II in the main text, in the cold ensemble, the rotating spinor image with the frequency of Ω actually scans in the azimuthal direction, while the individual off-axis atoms can "see" an amplitude-modulated probe field (*pulse train*). The carrier (central) frequency of the pulsed field is $(\omega_{+\ell}+\omega_{-\ell})/2=\omega_p$ and the modulation frequency is $\Delta\omega=(\omega_{+\ell}-\omega_{-\ell})/2=\ell\Omega$ where $\omega_{\pm\ell}=\omega_p\pm\ell\Omega$ are two Fourier frequencies (see Figs. 1(b), 1(c), and related work, e.g., in Refs. [39,43,44]). Therefore, for the light-atom interactions, our scheme is still in the context of slow-light model in the EIT system.

Following the work in Ref. [43], we can also make a formal and brief derivation for the susceptibilities $\chi(\omega_{\pm\ell})$ of the two Fourier frequencies $\omega_{\pm\ell}$ in the pulsed (bichromatic) probe field, which may provide empirical evidence to support the theoretical model in Sec. II in the main text. Due to the large temporal dispersion ($\partial\chi/\partial\omega\gg 1$) in the EIT system and the narrow spectral width $\Delta\omega=\ell\Omega\ll\omega_p$, the susceptibilities can be decomposed by Taylor expansion around the central frequency ω_p as

$$\chi(\omega_{\pm\ell})=\chi(\omega_p)+\sum_{\mathfrak{n}=1}^{+\infty}\frac{(\pm\ell\Omega)^{\mathfrak{n}}}{\mathfrak{n}!}\frac{\partial^{\mathfrak{n}}\chi}{\partial\omega^{\mathfrak{n}}}\bigg|_{\omega_p}, \tag{A1}$$

where we keep all the Taylor expansion orders. Note that, for long pulses with narrow spectral widths ($\Delta\omega=\ell\Omega\ll\omega_p$), it is usually not necessary to include higher-order expansions (e.g., only $\mathfrak{n}\leqslant 1$ terms are included in Ref. [43]). The susceptibility $\chi(\omega_p)$ of the monochromatic carrier field with the frequency ω_p has been fully studied in the tripod EIT system (see Ref. [42]) and can be given by

$$\chi(\omega_p)=\frac{i\mathcal{N}\mu_{14}^2}{\hbar\epsilon_0}\Big[(\gamma_{41}-i\Delta_p)+\frac{|\Omega_{c1}|^2}{(\gamma_{21}-i\delta')}+\frac{|\Omega_{c2}|^2}{(\gamma_{31}-i\delta'')}\Big]^{-1}, \tag{A2}$$

where one can refer back to Eqs. (1), (2), and Fig. 1(a) in the main text for the parameters. Therefore, the susceptibilities $\chi(\omega_{\pm\ell})$ of two Fourier frequencies $\omega_{\pm\ell}$ can be achieved by summing up the Taylor series in Eq. (A1), yielding

$$\chi(\omega_{\pm\ell})=\frac{i\mathcal{N}\mu_{14}^2}{\hbar\epsilon_0}\Big[(\gamma_{41}-i\Delta_{\pm\ell})+\frac{|\Omega_{c1}|^2}{(\gamma_{21}-i\delta'_{\pm\ell})}+\frac{|\Omega_{c2}|^2}{(\gamma_{31}-i\delta''_{\pm\ell})}\Big]^{-1}, \tag{A3}$$

where $\omega_{\pm\ell}=\omega_p\pm\ell\Omega$, $\Delta_{\pm\ell}=\Delta_p\pm\ell\Omega$, $\delta'_{\pm\ell}=\delta'\pm\ell\Omega$, and $\delta''_{\pm\ell}=\delta''\pm\ell\Omega$. This expression is well consistent with our result in Eq. (5) in the main text. Such a formal derivation of $\chi(\omega_{\pm\ell})$ based on the slow-light model could also provide an alternative to show the validity of the susceptibilities in Eq. (5).

APPENDIX B: A FORMAL DERIVATION OF n_g BASED ON THE STATIC SUSCEPTIBILITIES $\chi(\omega_{\pm\ell})$

As described above, due to the rotation of the image, the off-axis atoms actually experience an amplitude-modulated probe field (*pulse train*) with the central frequency ω_p and the modulation frequency $\Delta\omega=\ell\Omega$. This is still a slow-light scheme in the EIT system and the group refractive index n_g is one of the most characteristic parameters for the pulse dynamics. Moreover, as seen in the Pauli-like equation [i.e., Eq. (7)] in the main text, the group refractive index n_g is also critical to enhance the SOC strength ζ. In addition, note that, in other related work, e.g., the rotary photon drag model with similar optical configurations (images) to our scheme (see Refs. [40] and [44]), the group refractive index n_g in the so-called "specific rotary power" [consistent with the SOC strength ζ for $n_g\gg n\approx 1$ in Eq. (7)] is also formally derived from the static refractive indices of the two Fourier frequencies in the image.

It is reasonable to believe that the static and perturbative susceptibilities of the two Fourier frequencies ($\omega_{\pm\ell}$) could play a vital role in studying the slow-light effect of the pulsed probe field (i.e., the rotating spinor image) in the EIT system with large temporal dispersion. In what follows, considering the work in Ref. [43], we try to make a formal and brief derivation to show this fact. For the two Fourier frequencies, we have $\omega_{\pm\ell}=\omega_p\pm\Delta\omega$, $k_{\pm\ell}=k_p\pm\Delta k$, and the dispersion equations $k_{\pm\ell}c=\omega_{\pm\ell}n(\omega_{\pm\ell})$, which can lead to

$$\begin{aligned}2c\Delta k&=c(k_{+\ell}-k_{-\ell})=\omega_{+\ell}n(\omega_{+\ell})-\omega_{-\ell}n(\omega_{-\ell})\\&=(\omega_p+\Delta\omega)n(\omega_p+\Delta\omega)-(\omega_p-\Delta\omega)n(\omega_p-\Delta\omega)\\&=(\omega_p+\Delta\omega)\Big[n(\omega_p)+\Delta\omega\frac{\partial n}{\partial\omega}\Big]\\&\quad-(\omega_p-\Delta\omega)\Big[n(\omega_p)-\Delta\omega\frac{\partial n}{\partial\omega}\Big]\\&=2\omega_p\Delta\omega\frac{\partial n}{\partial\omega}+2\Delta\omega n(\omega_p),\end{aligned} \tag{B1}$$

where we expand the refractive indices as $n(\omega_p\pm\Delta\omega)=n(\omega_p)\pm\Delta\omega\frac{\partial n}{\partial\omega}|_{\omega_p}$ for the narrowband pulsed field with $\Delta\omega=\ell\Omega\ll\omega_p$. Using the definition of pulse group velocity (i.e., $v_g=\Delta\omega/\Delta k$) in Eq. (B1), we can find the group refractive index of the pulsed probe field with the central frequency ω_p and the modulation frequency $\Delta\omega$ as

$$n_g=\frac{c}{v_g}=n(\omega_p)+\omega_p\frac{\partial n}{\partial\omega}\bigg|_{\omega_p}, \tag{B2}$$

which agrees well with the result for slow-light studies in EIT systems with large temporal dispersion in Ref. [43]. Because $n=\sqrt{1+\chi}\approx 1+\chi/2$ for $\chi\ll 1$ in EIT systems, the static susceptibilities $\chi(\omega_{\pm\ell})$ of the two Fourier frequencies are of importance to determine the group velocity of the pulsed probe field.

Usually, in EIT systems, to find the group refractive index n_g of the pulsed probe field centered around the frequency ω_p, one can solve the static and perturbtive susceptibility $\chi(\omega_p)$ for a monochromatic field at the frequency ω_p and then use Eq. (B2) directly to find the group refractive index of the pulsed probe field. In our work, we actually focus on the origin of n_g (or v_g) in Eq. (B2) from the static and perturbative

susceptibilities of the two Fourier frequencies ($\omega_{\pm\ell}$) in the pulsed probe field [see Eq. (B1)].

As a simple justification, by using $\chi(\omega_{\pm\ell})$ resulting from the the steady-state solutions of the master equation [see Eqs. (1)–(6)] in the main text, it is straightforward to derive n_g of the pulsed probe field in the tripod system under the ideal EIT conditions with $\gamma_{21(31)} \approx 0$, $\Delta_{c1} = \Delta_{c2} = 0$, and $\Delta_{\pm\ell} = \pm\ell\Omega$ (i.e., without rotation, $\Delta_p = 0$). First, we have

$$\frac{\partial n}{\partial \omega} \approx \frac{n(\omega_{+\ell}) - n(\omega_{-\ell})}{\omega_{+\ell} - \omega_{-\ell}} \approx \frac{\chi(\omega_{+\ell}) - \chi(\omega_{-\ell})}{2(\omega_{+\ell} - \omega_{-\ell})} = \frac{\mathcal{N}\mu_{14}^2}{2\hbar\epsilon_0} \frac{1}{|\Omega_{c1}|^2 + |\Omega_{c2}|^2}. \tag{B3}$$

Because the central frequency ω_p of the pulsed probe field is resonant with the transition $|1\rangle \leftrightarrow |4\rangle$ in above situation ($\Delta_p = 0$), also combined with the conditions $\gamma_{21(31)} \approx 0$ and $\Delta_{c1} = \Delta_{c2} = 0$, we have the static susceptibility $\chi(\omega_p) = 0$, thus $n(\omega_p) = 1$. Finally, we can find the group refractive index

$$n_g = 1 + \frac{\mathcal{N}\mu_{14}^2}{2\hbar\epsilon_0} \frac{\omega_p}{|\Omega_{c1}|^2 + |\Omega_{c2}|^2}, \tag{B4}$$

which is in good agreement with the expression in Ref. [42] as well as that in Eq. (6) in the main text.

We also compare our work with Ref. [42]. In Ref. [42], the authors first achieve the static susceptibility at a single frequency, then directly use Eq. (B2) to find the group velocity (i.e., the group refractive index) of a narrowband amplitude-modulated probe field with the frequency range around the single central frequency. But, we here use the static susceptibilities $\chi(\omega_{\pm\ell})$ of the two Fourier frequencies to derive the group refractive index for the narrowband amplitude-modulated probe field. The two results are highly consistent with each other. Therefore, the static and perturbative susceptibilities $\chi(\omega_{\pm\ell})$ resulting from the the steady-state solutions of the master equation are still reliable to solve the slow-light-related issue in our proposal.

APPENDIX C: NUMERICAL ESTIMATIONS FOR THE PERTURBATION TERMS IN THE MASTER EQUATION

To numerically estimate the contributions of high-order terms in the master equation [see Eqs. (2)] in the main text, we consider some cases deviated from the ideal conditions used in Eqs. (2).

First, again following the work in Ref. [42] we assume that the system is initially prepared in a superposition of all energy levels as $|\psi(0)\rangle = \alpha_1|1\rangle + \alpha_2|2\rangle + \alpha_3|3\rangle + \alpha_4|4\rangle$, where $\alpha_{1,2,3,4}$ are the initial probability amplitudes. Based on the two-level model with the $|1\rangle \leftrightarrow |4\rangle$ transition, we roughly estimate the population ($\rho_{44} = |\alpha_4|^2$) in the excited state. The on-resonance population of state $|4\rangle$ can be given by $\rho_{44} = |\alpha_4|^2 = \frac{1}{2}s_0/(1 + s_0)$, where $s_0 = I_p/I_s$ is the on-resonance saturation parameter [52]. Because the intensity of the pulsed probe field I_p is much smaller than the saturation intensity I_s, we assume that the peak probe intensity $I_p^{\max} \approx 0.0002 I_s$ and thus find the maximum of ρ_{44} is about $\sim$0.0001. Note that, for a perfect dark state in EIT systems, due to the quantum interference effect in the presence of the strong coupling fields and other ground states, there could be even smaller population value ρ_{44} in the excited state.

Moreover, we assume $|\alpha_1|^2 \approx 0.99$, $|\alpha_2|^2 \approx 0.00495$, and $|\alpha_3|^2 \approx 0.00495$. Thus, to first order, we have $\rho_{11}(t) \approx |\alpha_1|^2 \approx 0.99$, $\rho_{44}(t) \approx |\alpha_4|^2 \approx 0.0001$, $\rho_{21}(t) \approx \alpha_2\alpha_1^* \approx 0.07$, $\rho_{31}(t) \approx \alpha_3\alpha_1^* \approx 0.07$, $\rho_{41}(t) \approx \alpha_4\alpha_1^* \approx 0.01$, $\rho_{24}(t) \approx \alpha_2\alpha_4^* \approx 0.0007$, and $\rho_{34}(t) \approx \alpha_3\alpha_4^* \approx 0.0007$ [42]. For simplicity, we here set $\alpha_{1,2,3,4}$ to be real numbers. Therefore, we have $\{\rho_{24}(t), \rho_{34}(t)\} \ll \{\rho_{41}(t), \rho_{31}(t), \rho_{21}(t)\}$ (at least an order of magnitude smaller). For a very weak probe light field, the terms $\Omega_p\rho_{24}$ and $\Omega_p\rho_{34}$ are so small (second-order small quantities) compared with the terms $\Omega_{c1}^*\rho_{41}$ and $\Omega_{c2}^*\rho_{41}$ in Eqs. (2) that they can be neglected.

Second, we further consider some special positions for the Bessel C1 field at the vicinity of the dark rings with vanishing intensity. Note that the Gaussian C2 field still exists in these regions. In this case, following the work in Ref. [53], we assume that the system is initially prepared in a superposition of two ground levels as $|\psi(0)\rangle = \alpha_1|1\rangle + \alpha_2|2\rangle$. At the dark rings of the Bessel C1 field, a new laser field could be generated at the transition $|2\rangle \leftrightarrow |4\rangle$ by the weak probe light field due to the parametric process studied in Ref. [53]. For $|\alpha_1|^2 \approx |\alpha_2|^2$, the new laser field could be significant. However, when we take $|\alpha_1|^2 \gg |\alpha_2|^2$ (e.g., $|\alpha_1|^2 \approx 0.9999$ and $|\alpha_2|^2 \approx 0.0001$) and also consider the near-resonance EIT conditions (i.e., $|\Omega_{c2}|^2 \gg \{\ell\Omega\gamma_{41}, \ell^2\Omega^2\}$ where Ω_{c1} is so weak that can be ignored at the dark rings of the Bessel C1 field) used in Eq. (6), based on the derivations in Ref. [53], the new laser at the transition $|2\rangle \leftrightarrow |4\rangle$ is much weaker than the probe field and thus can be neglected. In this case, the four-level tripod system can be reduced to a three-level Λ system. This fact is also reflected by the expression of the linear susceptibilities in Eq. (5). It means that, when the Bessel C1 field vanishes (i.e., $\Omega_{c1} \approx 0$) at the dark rings, Eq. (5) can be reduced to the linear susceptibilities for a three-level Λ system with the weak probe field and the strong coupling C2 field.

In general, our scheme is actually still a slow-light EIT model with an amplitude-modulated probe field (*pulse train*) experienced by the individual off-axis atoms in the cold ensemble. Based on the analyses above, it is seen that the initial preparation of the atomic levels is very crucial for the validity of deriving the susceptibility. As known, the preparation can be well controlled, for example, by using adiabatic passage techniques. As long as the conditions $\rho_{11} \approx 1$ and $\rho_{22} \approx \rho_{33} \approx \rho_{44} \approx 0$ can be satisfied, the parametric generation of new lasers can be suppressed and the EIT effect can be maintained, thus enabling large group refractive index n_g to enhance the SOC strength ζ in Eq. (7).

APPENDIX D: OTHER-ORDER TERMS ($\mathfrak{m} \neq \pm 1$) IN THE FLOQUET METHOD

As a matter of fact, the Floquet method is widely used for the EIT systems with bichromatic and even trichromatic light fields (e.g., see Refs. [54,55]). In these work, because the strong coupling fields are bichromatic or trichromatic, different Fourier components of the density matrix elements are always coupled with each other in the master equation

because the strong coupling fields cannot be ignored by perturbation theory. Hence, one must truncate the set of equations at high-order terms to achieve the required accuracy to calculate the atomic response to the probe field in the EIT systems.

However, in our scheme, instead of the strong bichromatic or trichromatic coupling fields, the weak probe field is bichromatic. As described before, for the light-atom interactions, our scheme is still in the context of the simplest slow-light model for the pulsed probe field (*pulse train*) in the EIT system. Accordingly, we adopt the perturbation theory widely used, for example, in Ref. [42] for a tripod EIT configuration.

Under perturbation theory in a slow-light model, the $\Omega_p\rho_{24}$ and $\Omega_p\rho_{34}$ terms can be negligible (also see Appendix C for some numerical estimations). Using the Floquet method, the equations for other-order ($\mathfrak{m} \neq \pm 1$) Fourier components can be simplified as

$$\dot{\rho}_{21}^{(\mathfrak{m})} = (-\gamma_{21} + i\delta'_{\pm\ell})\rho_{21}^{(\mathfrak{m})} + i\Omega_{c1}^{*}\rho_{41}^{(\mathfrak{m})}, \tag{D1a}$$

$$\dot{\rho}_{31}^{(\mathfrak{m})} = (-\gamma_{31} + i\delta''_{\pm\ell})\rho_{31}^{(\mathfrak{m})} + i\Omega_{c2}^{*}\rho_{41}^{(\mathfrak{m})}, \tag{D1b}$$

$$\dot{\rho}_{41}^{(\mathfrak{m})} = (-\gamma_{41} + i\Delta_{\pm\ell})\rho_{41}^{(\mathfrak{m})} + i\Omega_{c1}\rho_{21}^{(\mathfrak{m})} + i\Omega_{c2}\rho_{31}^{(\mathfrak{m})}. \tag{D1c}$$

Note that, because the effective probe Rabi frequency $\Omega_p = \Omega_{+\ell}e^{-i\ell\Omega t} + \Omega_{-\ell}e^{+i\ell\Omega t}$ in Eq. (1) in the main text is only associated with the $\pm$1st order harmonics of $\ell\Omega$, the $\Omega_{\pm\ell}$-related terms are missing in Eq. (D1) with $\mathfrak{m} \neq \pm 1$. Taking the steady state limit, we assume $\dot{\rho}_{21}^{(\mathfrak{m})} = \dot{\rho}_{31}^{(\mathfrak{m})} = \dot{\rho}_{41}^{(\mathfrak{m})} = 0$ on the left side of the equations. It is seen that a set of homogeneous linear equations for $\rho_{21}^{(\mathfrak{m})}$, $\rho_{31}^{(\mathfrak{m})}$, and $\rho_{41}^{(\mathfrak{m})}$ ($\mathfrak{m} \neq \pm 1$) can be derived and the determinant of coefficient matrix is usually nonzero. As a result, the matrix elements $\rho_{21}^{(\mathfrak{m})}$, $\rho_{31}^{(\mathfrak{m})}$, and $\rho_{41}^{(\mathfrak{m})}$ ($\mathfrak{m} \neq \pm 1$) should be zero. Therefore, we only retain the nonzero $\pm$1st-order terms $\rho_{21}^{(\mp 1)}$, $\rho_{31}^{(\mp 1)}$, and $\rho_{41}^{(\mp 1)}$ as seen in Eqs. (4) and the results in Eqs. (5) and (6) are also consistent with those obtained in the slow-light EIT model with a weak probe field.

[1] S. E. Harris, Electromagnetically induced transparency, Phys. Today **50**, 36 (1997).

[2] M. D. Lukin, *Colloquium:* Trapping and manipulating photon states in atomic ensembles, Rev. Mod. Phys. **75**, 457 (2003).

[3] M. Fleischhauer, A. Imamoğlu, and J. P. Marangos, Electromagnetically induced transparency: Optics in coherent media, Rev. Mod. Phys. **77**, 633 (2005).

[4] L. Zhao, T. Wang, Y. Xiao, and S. F. Yelin, Image storage in hot vapors, Phys. Rev. A **77**, 041802(R) (2008).

[5] P. K. Vudyasetu, R. M. Camacho, and J. C. Howell, Storage and Retrieval of Multimode Transverse Images in Hot Atomic Rubidium Vapor, Phys. Rev. Lett. **100**, 123903 (2008).

[6] L. Zhao, G. Yang, and W. Duan, Manipulating stored images with phase imprinting at low light levels, Opt. Lett. **37**, 2853 (2012).

[7] J. Wu, Y. Liu, D.-S. Ding, Z.-Y. Zhou, B.-S. Shi, and G.-C. Guo, Light storage based on four-wave mixing and electromagnetically induced transparency in cold atoms, Phys. Rev. A **87**, 013845 (2013).

[8] L. Zhao, W. Duan, and S. F. Yelin, All-optical Fresnel lens in coherent media: Controlling image with image, Opt. Express **19**, 981 (2011).

[9] H. Y. Ling, Y.-Q. Li, and M. Xiao, Electromagnetically induced grating: Homogeneously broadened medium, Phys. Rev. A **57**, 1338 (1998).

[10] M. Mitsunaga and N. Imoto, Observation of an electromagnetically induced grating in cold sodium atoms, Phys. Rev. A **59**, 4773 (1999).

[11] P.-W. Zhai, X.-M. Su, and J.-Y. Gao, Optical bistability in electromagnetically induced grating, Phys. Lett. A **289**, 27 (2001).

[12] G. C. Cardoso and J. W. R. Tabosa, Electromagnetically induced gratings in a degenerate open two-level system, Phys. Rev. A **65**, 033803 (2002).

[13] B. K. Dutta and P. K. Mahapatra, Electromagnetically induced grating in a three-level Ξ-type system driven by a strong standing wave pump and weak probe fields, J. Phys. B **39**, 1145 (2006).

[14] Z.-H. Xiao, S. G. Shin, and K. Kim, An electromagnetically induced grating by microwave modulation, J. Phys. B **43**, 161004 (2010).

[15] R.-G. Wan, J. Kou, L. Jiang, Y. Jiang, and J.-Y. Gao, Electromagnetically induced grating via enhanced nonlinear modulation by spontaneously generated coherence, Phys. Rev. A **83**, 033824 (2011).

[16] L. Wang, F. Zhou, P. Hu, Y. Niu, and S. Gong, Two-dimensional electromagnetically induced cross-grating in a four-level tripod-type atomic system, J. Phys. B **47**, 225501 (2014).

[17] L. Zhao, W. Duan, and S. F. Yelin, All-optical beam control with high speed using image-induced blazed gratings in coherent media, Phys. Rev. A **82**, 013809 (2010).

[18] S. A. Carvalho and L. E. E. de Araujo, Electromagnetically induced blazed grating at low light levels, Phys. Rev. A **83**, 053825 (2011).

[19] S. Kuang and H. Yang, Blazed gain grating in a four-level atomic system, J. Opt. Soc. Am. B **30**, 136 (2013).

[20] Y.-Y. Chen, Z.-Z. Liu, R.-G. Wan, Beam splitter and router via an incoherent pump-assisted electromagnetically induced blazed grating, Appl. Opt. **56**, 5736 (2017).

[21] L. E. E. de Araujo, Electromagnetically induced phase grating, Opt. Lett. **35**, 977 (2010).

[22] S. A. Carvalho and L. E. E. de Araujo, Electromagnetically-induced phase grating: A coupled-wave theory analysis, Opt. Express **19**, 1936 (2011).

[23] L. Zhao, W. Duan, and S. F. Yelin, Generation of tunable-volume transmission-holographic gratings at low light levels, Phys. Rev. A **84**, 033806 (2011).

[24] L. Zhao, Vortex-based all-optical manipulation of stored light at low light levels, Opt. Express **23**, 29808 (2015).

[25] S. Asghar, Ziauddin, S. Qamar, and S. Qamar, Electromagnetically induced grating with Rydberg atoms, Phys. Rev. A **94**, 033823 (2016).

[26] J. Yuan, S. Dong, C. Wu, L. Wang, L. Xiao, and S. Jia, Optically tunable grating in a $V + \Xi$ configuration involving a Rydberg state, Opt. Express **28**, 23820 (2020).

[27] L. Zhao, Electromagnetically induced polarization grating, Sci. Rep. **8**, 3073 (2018).
[28] Y.-M. Liu, F. Gao, C.-H. Fan, and J.-H. Wu, Asymmetric light diffraction of an atomic grating with $\mathscr{P}\mathscr{T}$ symmetry, Opt. Lett. **42**, 4283 (2017).
[29] T. Shui, W.-X. Yang, S. Liu, L. Li, and Z. Zhu, Asymmetric diffraction by atomic gratings with optical $\mathscr{P}\mathscr{T}$ symmetry in the Raman-Nath regime, Phys. Rev. A **97**, 033819 (2018).
[30] C. Hang, W. Li, and G. Huang, Nonlinear light diffraction by electromagnetically induced gratings with $\mathscr{P}\mathscr{T}$ symmetry in a Rydberg atomic gas, Phys. Rev. A **100**, 043807 (2019).
[31] F. Cardano and L. Marrucci, Spin-orbit photonics, Nat. Photonics **9**, 776 (2015).
[32] K. Y. Bliokh, F. J. Rodriguez-Fortuno, F. Nori, and A. V. Zayats, Spin-orbit interactions of light, Nat. Photonics **9**, 796 (2015).
[33] L. Zhao, All-optical spin-orbit coupling of light using electromagnetically induced transparency, Phys. Rev. A **100**, 013832 (2019).
[34] L. Zhao, All-optical spin-orbit coupling of light in coherent media using rotating image, Ann. Phys. **532**, 1900371 (2020).
[35] L. Allen, M. W. Beijersbergen, R. J. C. Spreeuw, and J. P. Woerdman, Orbital angular momentum of light and the transformation of Laguerre-Gaussian laser modes, Phys. Rev. A **45**, 8185 (1992).
[36] J. Durnin, J. J. Miceli, and J. H. Eberly, Diffraction Free Beams, Phys. Rev. Lett. **58**, 1499 (1987).
[37] D. McGloin and K. Dholakia, Bessel beams: Diffraction in a new light, Contemp. Phys. **46**, 15 (2005).
[38] J. Courtial, K. Dholakia, D. A. Robertson, L. Allen, and M. J. Padgett, Measurement of the Rotational Frequency Shift Imparted to a Rotating Light Beam Possessing Orbital Angular Momentum, Phys. Rev. Lett. **80**, 3217 (1998).
[39] S. Franke-Arnold, J. Leach, M. J. Padgett, V. E. Lembessis, D. Ellinas, A. J. Wright, J. M. Girkin, P. Öhberg, and A. S. Arnold, Optical ferris wheel for ultracold atoms, Opt. Express **15**, 8619 (2007).
[40] J. Leach, A. J. Wright, J. B. Götte, J. M. Girkin, L. Allen, S. Franke-Arnold, S. M. Barnett, and M. J. Padgett, "Aether Drag" and Moving Images, Phys. Rev. Lett. **100**, 153902 (2008).
[41] M. O. Scully and M. S. Zubairy, *Quantum Optics* (Cambridge University Press, Cambridge, UK, 1997).
[42] E. Paspalakis and P. L. Knight, Transparency, slow light and enhanced nonlinear optics in a four-level scheme, J. Opt. B: Quantum Semiclass. Opt. **4**, S372 (2002).
[43] A. B. Matsko, O. Kocharovskaya, Y. Rostovtsev, G. R. Welch, A. S. Zibrov, and M. O. Scully, Slow, ultraslow, stored, and frozen light, Adv. At., Mol., Opt. Phys. **46**, 191 (2001).
[44] J. B. Götte, S. M. Barnett, and M. J. Padgett, On the dragging of light by a rotating medium, Proc. R. Soc. A **463**, 2185 (2007).
[45] Z. Ficek and H. S. Freedhoff, VI Spectroscopy in polychromatic fields, Prog. Opt. **40**, 389 (2000).
[46] M. A. Player, On the dragging of the plane of polarization of light propagating in a rotating medium, Proc. R. Soc. London A Math. Phys. Sci. **349**, 441 (1976).
[47] D. A. Steck, Rubidium 87 D Line Data, available online at http://steck.us/alkalidata (revision 2.1.4, 23 December 2010).
[48] R. V. Jones, Rotary "aether drag," Proc. R. Soc. London A Math. Phys. Sci. **349**, 423 (1976).
[49] Y. Wang, J. Li, S. Zhang, K. Su, Y. Zhou, K. Liao, S. Du, H. Yan, and S.-L. Zhu, Efficient quantum memory for single-photon polarization qubits, Nat. Photonics **13**, 346 (2019).
[50] D. G. Grier, A revolution in optical manipulation, Nature (London) **424**, 810 (2003).
[51] R. Ficklera, G. Campbelld, B. Buchlerd, P. K. Lamd, and A. Zeilinger, Quantum entanglement of angular momentum states with quantum numbers up to 10, 010, Proc. Natl. Acad. Sci. USA **113**, 13642 (2016).
[52] H. J. Metcalf and P. van der Straten, *Laser Cooling and Trapping* (Springer-Verlag, New York, 1999).
[53] E. Paspalakis and P. L. Knight, Transparency and parametric generation in a four-level system, J. Mod. Opt. **49**, 87 (2002).
[54] J. Wang, Yifu Zhu, K. J. Jiang, and M. S. Zhan, Bichromatic electromagnetically induced transparency in cold rubidium atoms, Phys. Rev. A **68**, 063810 (2003).
[55] X.-M. Hu, J.-H. Zou, X. Li, D. Du, and G.-L. Cheng, Amplitude and phase control of trichromatic electromagnetically induced transparency, J. Phys. B: At. Mol. Opt. Phys. **38**, 683 (2005).